TECHNICAL ARTICLE

Effects of resolution in real and reciprocal spaces from a 2D detector at a high-energy synchrotron beamline

Andrea Bernasconi[1,a] and Jonathan Wright[2]
[1]*Università di Pavia, Pavia, Italy*
[2]*ESRF – The European Synchrotron, Grenoble, France*

(Received 27 July 2017; accepted 24 October 2017)

Different experimental conditions at a versatile high-energy beamline equipped with a two-dimensional detector have been compared for powder diffraction and pair distribution function (PDF) experiments. In particular, sample size and sample to detector distances have been evaluated on a standard sample, to evaluate their effects in both Q and real space. Two illustrative cases are also discussed. The average structure and local distortions in a $BaTiO_3$ powder with 100 nm particle size show that spurious ripples in the PDF are suppressed by increased counting statistics. Effects of small amounts of a crystalline impurity phase on a SiO_2.Al_2O_3.Na_2O.CaO glass have been quantified.
 [doi:10.1017/S0885715617001166]

Key words: 2D detector, pair distribution function, synchrotron, Q-resolution

I. INTRODUCTION

Synchrotron powder diffraction is a well-understood technique to probe the structure of materials for purposes like structure determination and/or refinement, *in situ* characterization, or trace phase quantification. Experiments should be designed to be as sensitive as possible to the details of interest for a specific problem. Because of this, versatility is a key feature for a modern diffraction instrument. While flexibility is appealing, practicality and quality of the results also need to be preserved. The focus of the present study is synchrotron X-ray diffraction with two-dimensional (2D) detectors where there are many parameters which can be varied. An incident photon energy should be chosen to suit both the chemical composition of the sample and the Q-range to be measured. Increasing sample to detector distance improves the reciprocal space resolution, which can be good for monitoring phase transitions which involve a lattice distortion or for following an evolving quantitative phase analysis, but with the drawback that it reduces the Q-range and count rate per pixel (Norby, 1997). Placing the detector as close as possible increases the Q-range which improves real-space resolution for pair distribution function, or PDF, methods (Egami and Billinge, 2003).

Recent developments in X-ray focusing optics mean it is now possible to create X-ray beams with sizes ranging from nanometers to millimeters (Kirkpatrick and Baez, 1948; Snigirev *et al.*, 2009; Vaughan *et al.*, 2011; Cesar Da Silva *et al.*, 2017). The bandpass ($\Delta E/E$) of the X-ray beam can even be chosen by selecting different optics or changing the bending of a curved crystal monochromator. Features of the detector, like point spread function (PSF), can also be controlled (e.g. by binning or changing a phosphor screen). Because of this versatility, experimental conditions are multiple and the measured data depend on a convolution of all of these effects. Although the qualitative effect of many parameters on the resultant diffraction pattern is well known, in the first part of this paper, we have computed their effects by geometrical derivation, before checking the results on a reference material.

The second part of this paper shows two examples of applications where the choice of experimental parameters was not obvious: how best to detect small distortions in a material with a small particle size and how to deal with mixtures of crystalline and amorphous samples? The first example is the case of a barium-perovskite ($BaTiO_3$) with a particle size of about 100 nm, a material which has been intensively studied for its piezoelectric and ferroelectric applications (Chandler *et al.*, 1993; Bhalla *et al.*, 2000). Several temperature-dependent crystallographic transitions are well established from the literature (Kwei *et al.*, 1993). $BaTiO_3$ is cubic at high temperatures, exhibiting a paraelectric behavior down to 393 K. At lower temperature it converts to tetragonal (until 278 K), then orthorhombic (until 183 K), and then rhombohedral structures at lower temperatures. All of these three modifications are characterized by the off-centering of titanium species from the octahedral units, which causes ferroelectric behavior.

The second example is the case of a SiO_2.Al_2O_3.Na_2O.CaO glass, a material whose network is made by corner-sharing structural units (i.e. silicon and aluminum centered tetrahedra) which is interrupted by network modifier cations, like calcium and sodium. The modifiers have strong implications on the technological properties of the material because the structure changes its degree of polymerization (Shelby, 2005). High-energy X-ray diffraction capabilities to probe non-crystalline materials have already been well established (Yavari *et al.*, 2005; Bernasconi *et al.*, 2016); therefore, our goal is removing the effect of progressive additions of crystalline SiO_2 quartz to the original glass sample. This approach can be of interest in the field of ceramic materials when dealing with glazes whose microstructure is dominated (more than 90 wt. %) by a glassy matrix (Bernasconi *et al.*, 2012), or to follow glass structure evolution in the presence of recrystallization.

[a]Author to whom correspondence should be addressed. Electronic mail: andrea.bernasconi@unipv.it

II. EXPERIMENTAL SECTION

Experiments have been performed at the material science beamline ID11 (ESRF, Grenoble). The diffraction data have been acquired in transmission geometry, with a fast readout fiber optic coupled CCD detector (Frelon camera, 2048 × 2048 pixels, 16 bits, Labiche *et al.,* 2007) with a pixel size of 50 µm. All the investigated samples were rotating during the data acquisition, with the exception of the glass with crystalline phase impurity. We have divided the rest of this section and the next section into three different parts: the instrument resolution, the nanocrystalline $BaTiO_3$ powder, and the mixed crystalline/amorphous sample.

A. Instrumental resolution

We have verified the Q (reciprocal space) and r (real space) resolution by measuring silicon NIST SRM640c powder using different capillary diameters and sample to detector distances. Two common diameters of Kapton capillaries have been selected (0.5 and 1.5 mm) and three sample to detector distances have been chosen (9, 12, and 22 cm). The X-ray beamsize was around 75 µm square and defined by slits. For each configuration, ten images with an exposure time of 3 s have been collected and then averaged to improve the counting statistics. Ten empty capillary images were collected as well, to be able to subtract the background and eventually generate a PDF (described below). For configurations with the shorter detector distances of 9 and 12 cm, the detector was offset to maximize the Q-range by putting the beam center in the corner of the image, and keeping the edge of the camera vertical. This has the drawback that only quarter of rings have been measured instead of full rings, but it gives a factor of almost 2 increase of the Q-range and the azimuth range still averages over horizontal and vertical beam polarizations. This experiment was performed at the Hf K-edge energy (65.352 keV).

B. One hundred nanometer grain-sized $BaTiO_3$

A nanocrystalline material from Aldrich (CAS 12047-27-7) whose particle size is around 100 nm from Brunauer-Emmett-Teller (BET) analysis was loaded into a borosilicate glass capillary (diameter of 0.5 mm). Data were collected with wavelength $\lambda = 0.12465$ Å ($E \sim 100$ keV) with a sample detector distance of around 15 cm for reciprocal space analysis to give Q_{MAX} around 8 $Å^{-1}$. Further data with a sample detector distance of 8.7 cm were collected for real space analysis (Q_{MAX} around 31 $Å^{-1}$) at the Pt K-edge energy (78.395 keV). Five hundred images with an exposure time of 5 s/image have been collected to provide extremely good counting statistics for the PDF analysis. The same data collection strategy was adopted to measure the empty capillary.

C. Glass with crystalline phase impurity

Small quartz additions have been performed on a complex aluminosilicate-based glass (composition in weight % is 69.69 SiO_2, 13.54 Al_2O_3, 7.06 CaO, and 11.71 Na_2O) obtained by quenching from 1200 °C. Full compositions are given in Table I. After a preliminary homogenization of the amorphous and crystalline phases by gently grinding in an agate mortar, each composition was loaded into a Kapton capillary (diameter of 1.5 mm) and then measured at the beamline at an energy of 60 keV (λ equals to 0.20535 Å). The larger capillary diameter of 1.5 mm (c.f. 0.5 mm for $BaTiO_3$) was selected to enhance the weak signal at the expense of some Q resolution; a high Q resolution is not as important when studying glassy samples. A sample detector distance of 8.5 cm has been chosen to correspond to a Q_{MAX} of about 23.5 $Å^{-1}$. For each composition, five different positions along the capillary have been measured to increase sampling statistics (for the glass) and to improve the effectiveness of our further data processing by median filtering of the five different regions per sample. Then 500 images of 0.5 s were collected for each region. The short exposure time was selected to avoid saturation of the detector because of strong Bragg's single-crystal diffraction of quartz, while the large number of images overcomes statistical noise. For the empty capillary, 500 images of 0.5 s of exposure time were collected as well.

TABLE I. Quartz wt. % addition to the glass phase.

Sample name	Quartz wt. %	Packing fraction	Sample density (g cm^{-3})
GL0	0	0.352	2.469
GL1	1.21	0.368	2.471
GL2	2.45	0.336	2.473
GL3	3.19	0.409	2.475
GL4	4.33	0.408	2.477
GL5	5.39	0.355	2.479
GL6	6.48	0.311	2.481
GL7	7.85	0.386	2.483
GL8	8.64	0.342	2.485
GL9	9.95	0.309	2.487
GL10	11.35	0.323	2.490

Experimental packing fractions are also provided as well as sample density, considering a density of 2.469 and 2.65 g cm^{-3} for glass and quartz, respectively.

D. Data processing

The momentum transfer Q can be computed from Bragg's law as:

$$Q = \frac{4\pi}{\lambda} \sin\left(\frac{\arctan(R/D)}{2}\right) \quad (1)$$

where λ is the incident wavelength, R is the active radius of the 2D detector, and D is the sample to detector distance. For these measurements, the incident beam was focused by Al and Be lenses in an in-vacuum transfocator to increase the flux density at the sample position (Vaughan *et al.*, 2011). The images have been processed using the pyFAI software (Kieffer and Wright, 2013) to get the 2θ-intensity profile. An incident angle correction (Wu *et al.*, 2002; Bernasconi *et al.*, 2015) has been applied using previously measured X-ray phosphor transmission values (in the range 0.6–0.8 at these energies). Before transformation to real space, the data also need to be corrected for contributions from the empty capillary, Compton scattering, and self-absorption, in order to obtain the coherent intensity I_C. This quantity is normalized to the average X-ray atomic form factor of the sample in order to get the total scattering function $S(Q)$ using the equation:

$$S(Q) = \frac{I_C - \langle f(Q^2)\rangle + \langle f(Q)\rangle^2}{\langle f(Q)\rangle^2} \quad (2)$$

https://doi.org/10.1017/S0885715617001166 Published online by Cambridge University Press

This function is Fourier transformed to give the reduced pair distribution function $G(r)$ or the pair distribution function $g(r)$ by the equation:

$$G(r) = 4\pi\rho_0 r(g(r) - 1) = \frac{2}{\pi}\int_0^\infty Q[S(Q) - 1]\text{sine}(Qr)dQ \quad (3)$$

where ρ_0 is the average number density of the material. PDFgetX3 (Juhas *et al.*, 2013) and GudrunX (Soper, 2010a, b) are software packages which can be used to carry out these steps.

In the cases of silicon NIST SRM640c and 100 nm grain-sized $BaTiO_3$, the PDFgetX3 was used. This software works well for crystalline and even nanostructured materials. In the case of glass plus crystalline phase, GudrunX was used instead as it allowed us better control of the various parameters and what is signal vs. background.

III. RESULTS AND DISCUSSION

A. *Q*-space resolution effects

We look at the effect of some parameters on the Q-space resolution of a 2D detector. Consider a sample with thickness t, irradiated by a parallel beam, whose size is b, located at a distance D from the area detector, whose PSF is ps. The wavelength λ is not unique because of the bandpass bp of the monochromator. Figure 1 represents the geometry of the diffraction experiment in the absence of detector tilts, where also the footprint F of the beam diffracted by the sample, at a given 2θ angle, is shown.

To compute the Q-space resolution, the quantity between the Q values at the end of the footprint, for a given 2θ angle, needs to be considered. This quantity, which we will call as deltaQ, corresponds to the difference between the two lengths $R1$ and $R2$. $R1$ is the distance between the beam center on the detector and the inner point of the diffracted beam on the detector, which is related to the inner front of the sample, corresponding to:

$$R1 = \tan(2\theta)\left(D - \frac{t}{2}\right) - \frac{b}{2} - \frac{ps}{2} \quad (4)$$

$R2$ is the distance between the beam center on the detector and the outer point of the diffracted beam on the detector, which is related to the outer back of the sample, corresponding to:

$$R2 = \tan(2\theta)\left(D + \frac{t}{2}\right) + \frac{b}{2} + \frac{ps}{2} \quad (5)$$

When moving these quantities in Q-space from 2θ space by substitution with Eq.(1), one should consider the bandpass effect which implies a reduction of $R1$ because of the smaller wavelength tail of the beam (i.e. λ_{LOW}) and a raise of $R2$ because of the higher wavelength tail of the beam (i.e λ_{HIGH}). So deltaQ corresponds to:

$$\text{delta}Q = \frac{4\pi}{\lambda_{\text{low}}}\sin\left(\frac{\arctan\left((R2/D)\right)}{2}\right) - \frac{4\pi}{\lambda_{\text{high}}}\sin\left(\frac{\arctan\left((R1/D)\right)}{2}\right) \quad (6)$$

The quantities λ_{LOW} and λ_{HIGH} correspond to (λ–bp λ) and (λ + bp λ), respectively. Figure 2 displays the behavior of deltaQ by varying its controlling parameters t, b, ps, bp, λ, and D, starting from an initial configuration where these values correspond to 0.5 mm, 75 µm, four pixels (assuming a pixel size of 50 µm), 2×10^{-3}, 0.1899 Å and 9 cm, respectively.

The Q-resolution is clearly improved by:

(i) a thinner sample (blue vs. green curves);
(ii) a smaller beamsize (blue vs. gray curves);
(iii) a narrower PSF (blue vs. red curves);
(iv) a lower bandpass (blue vs. black curves);
(v) a larger sample to detector distance giving a smaller Q_{MAX} (blue vs. orange curves);
(vi) a longer wavelength giving a smaller Q_{MAX} (blue vs. cyan curves).

Points i–v all reduce the signal. The effect of wavelength is less obvious as it depends on the incident spectrum, sample absorption and required Q_{MAX} and the intrinsic sample cross-sections for Compton vs. Thompson scattering.

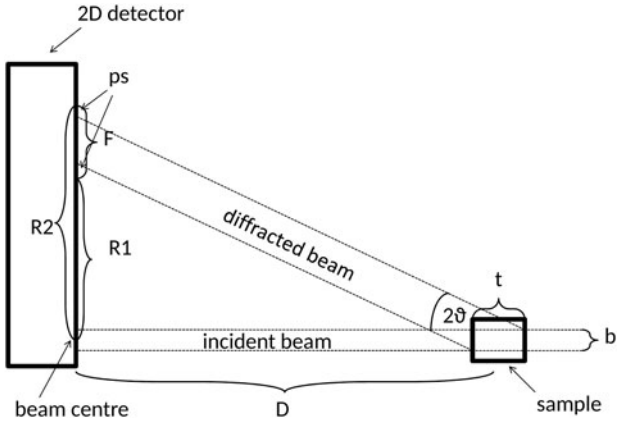

Figure 1. Geometry of the diffraction experiment in transmission with a 2D detector.

B. Experimental resolution

A total of six configurations have been explored by changing capillary size and sample to detector distance. To compare their different Q-resolution, the full width at half maximum (FWHM) of each peak has been extracted by using a Pearson VII function (Hall *et al.*, 1977). The true peak shape depends on the detector PSF (Holton *et al.*, 2012) and beam shape and this goes beyond the scope of the current work where we focus on the FWHM resolution.

By considering these experimental results, it is possible to check the previous calculations from Eq. (6). The measured FWHM was only one choice of a peak width parameter, other measures like integral breadth (etc.) are also possible and a more detailed ray-tracing computation might reveal the precise peak shape. For simplicity, we compared the FWHM from the data as half of deltaQ (e.g. we approximate the peak as a triangle where deltaQ is the length of the base). Figure 3 shows the FWHMs of the six investigated

https://doi.org/10.1017/S0885715617001166 Published online by Cambridge University Press

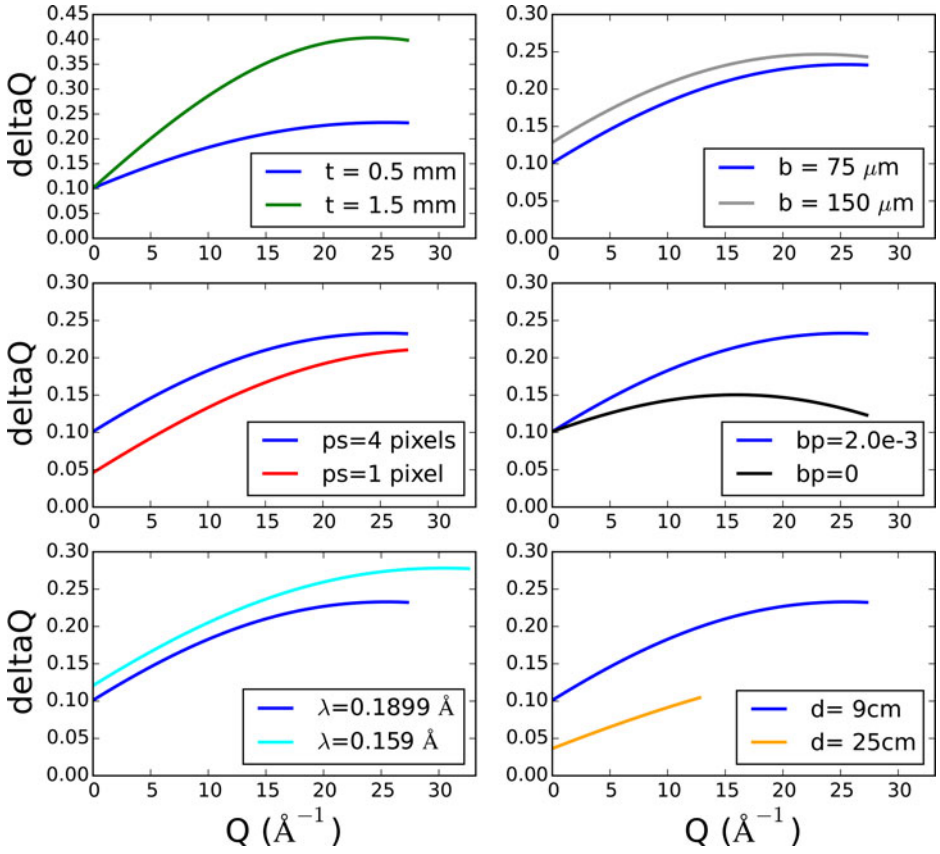

Figure 2. (Colour online) Computed effects of different parameters on deltaQ as defined from Eq. (6). Initial configuration (i.e. blue curve) corresponds to a sample thickness of 0.5 mm, a beamsize of 75 μm, a point spread of 4 pixels (assuming a pixel size of 50 μm, a bandpass of $2*10^{-3}$, a wavelength of 0.1899 Å, and a sample to detector distance of 9 cm. Variations from this initial configuration are described in the different legends.

configurations vs. Q, and deltaQ/2 from Eq. (6). A good general agreement was found. In the calculations, beamsize, PSF, bandpass, and wavelength were 75 μm, 4 pixels (assuming a pixel size of 50 μm), 2×10^{-3}, and 0.1899 Å.

It is not intuitive to evaluate these effects in real space. We have excluded the largest detector distance (i.e. 22 cm) because Q_{MAX} would be too low for a meaningful real space analysis (i.e. 7.5 Å^{-1}). For the other data, we have compared the $G(r)$ real space resolution and the damping at high r values, which depends on the exponential of $\delta Q^2 r^2/2$ (Proffen *et al.*, 2005). In this case of silicon NIST SRM 640c, the best real space resolution is provided by the data which have the largest Q-range (about 24 Å^{-1}) as seen in Figure 4 (left side).

The resolution improvement (blue curves) allows weaker peaks at 10.42, 11.76, and 12.15 Å to be distinguished from the strong neighbors at 10.16, 11.52, and 12.37 Å, respectively. These features are not clear in the data collected with Q_{MAX} of 20 Å^{-1} in the green curves. The damping of $G(r)$ is reduced in the data with lower Q-range and smaller capillary size (see Figure 4, right side, green curve with triangles), because of the improved Q-resolution. The data with the largest Q-range have the most damped signal (blue curve with circles). We have evaluated $G(r)$ features using the PDFGUI program (Farrow *et al.*, 2007) in terms of Q_{DAMP} and Q_{BROAD} parameters in the 1–40 Å real space range. This range has been selected as region where $G(r)$ clearly shows features for all four configurations. In the refinement strategy, the silicon isotropic thermal displacement parameter (i.e. U_{ISO} in PDFGUI) has been kept fixed at 0.0056 Å^2 (from a previous Rietveld determination using data collected at the high-resolution beamline, ID22, ESRF). Correlated atomic motion effects have been also considered in the modeling (Jeong *et al.*, 2003). The results of these fits are summarized in Figure 5, where a very good fit is displayed for all four configurations.

Although the damping is well modeled by the fitting routine, we have quantified how it affects the accuracy of the results. To compare the four configurations, silicon coordination numbers have been extracted by integrating the radial distribution function $R(r)$ in a range of interest:

$$R(r) = G(r)r + 4\pi r^2 \rho_0$$

Coordination numbers have been calculated by normalizing the integral of the second peak in $G(r)$ to be 12 for all four experimental conditions. The value 12 is because of the silicon structure (space group *Fd-3m*), and all the other integrals have been scaled in the same way. The second peak is preferred to the first because there are fewer spurious ripples which may bias the values. The results are displayed in Figure 6.

A general good agreement has been found, with the better accuracy provided by the data collected with the larger capillary size and with the higher Q-range (blue circles in Figure 6) in the 1–7 Å range (average error is 7.49%). At short radius values, the real space resolution (larger Q-range) and higher counting statistics (larger sample) are more important. However, if the 7–11 Å range is considered, better accuracy

https://doi.org/10.1017/S0885715617001166 Published online by Cambridge University Press

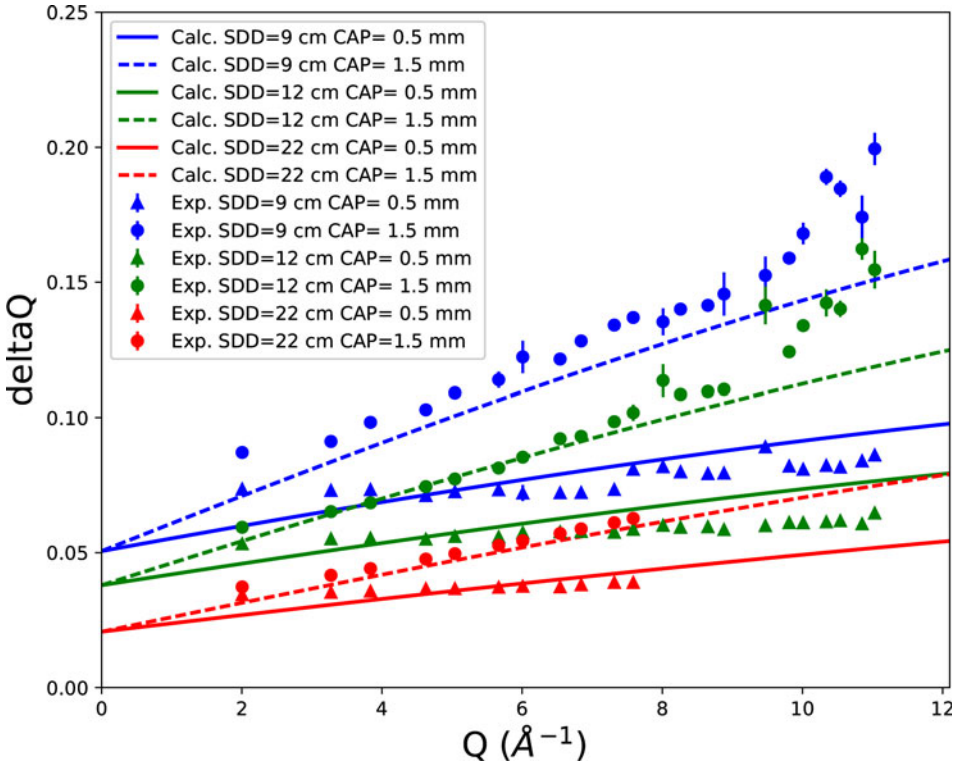

Figure 3. (Colour online) Measured FWHMs of the six investigated configurations versus Q (symbols) and deltaQ/2 from Eq. (6) (lines).

(average error is 9.85%) is provided by the data with a smaller capillary size and a higher *Q*-range (blue triangles in Figure 6). Increasing the *Q*-range has helped in both cases, but a larger sample degrades the results at higher *r* values because of increased damping. Full results are summarized in Table II. Our coordination analysis does not go beyond the values of 11 Å because of peak of overlaps. We conclude that the results are useful provided that (i) the statistics are good enough to avoid spurious ripples for first coordination shells and (ii) the signal is not damped for further shells. Moreover, accuracy is improved by increasing the *Q*-range.

C. One hundred nanometer grain-sized $BaTiO_3$

We started our analysis with Rietveld refinement by using the Topas program (Coelho, 2005). Tetragonal (space group *P*4*mm*) and cubic (space group *Pm*-3*m*) crystallographic modifications have been used to model the data. Because oxygen

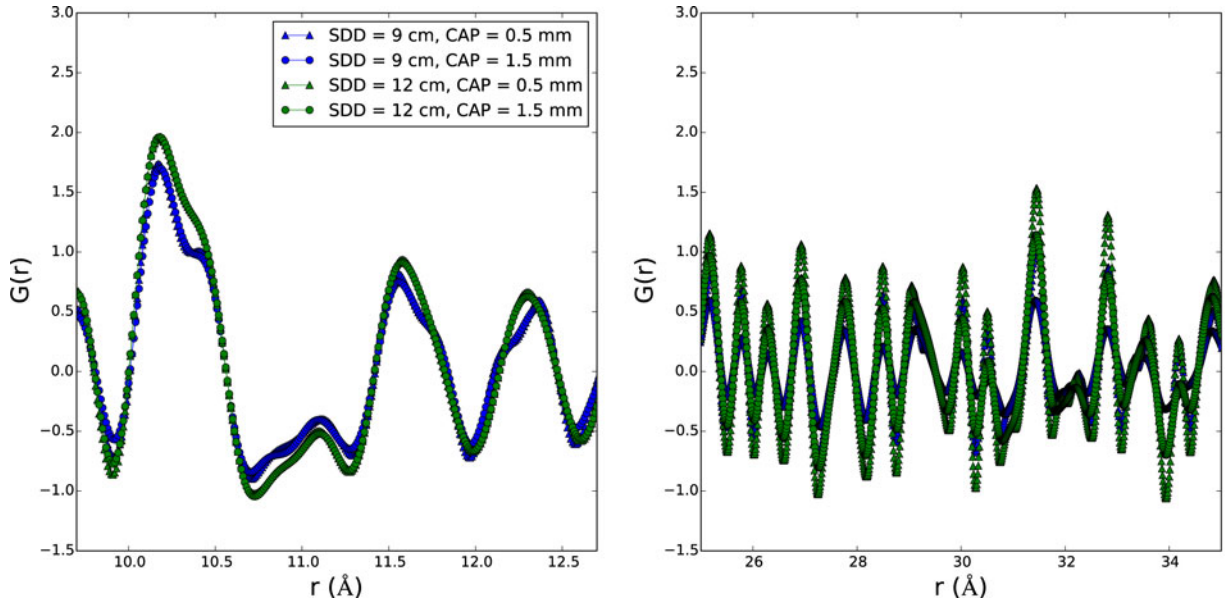

Figure 4. (Colour online) Silicon NIST SRM 640c *G(r)*s for different Qrange and capillary size. On the left the real space resolution is displayed. On the right side the real space dampening is displayed. For blue curve the Q_{MAX} is about 24 Å^{-1} while for green curves Q_{MAX} is about 20 Å^{-1}.

https://doi.org/10.1017/S0885715617001166 Published online by Cambridge University Press

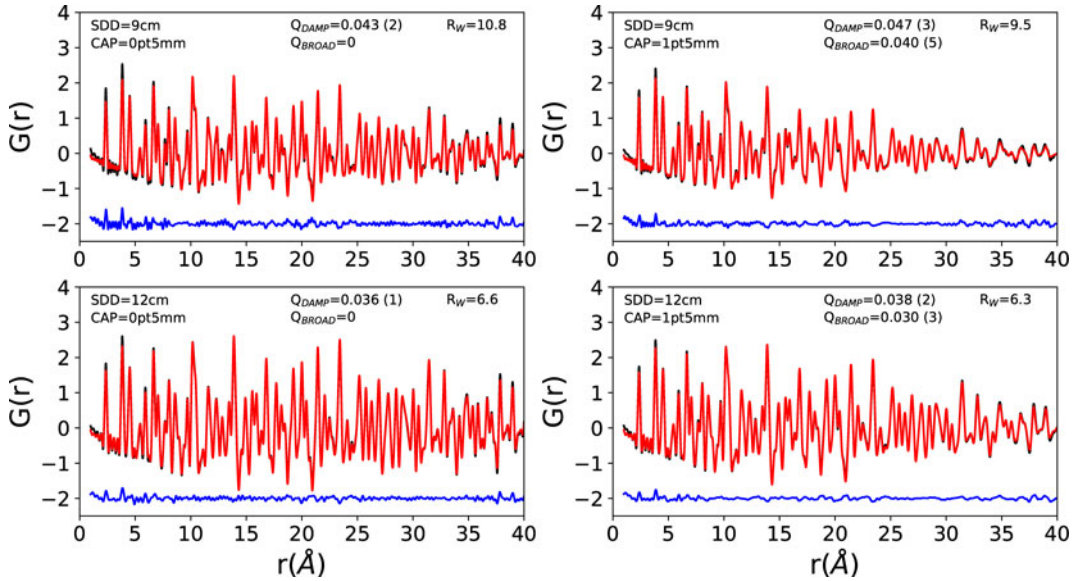

Figure 5. (Colour online) PDFGUI silicon NIST SRM 640c *G(r)* graphic fit for all the different investigated sample to detector distances and capillary size conditions. Q_{DAMP} and Q_{BROAD} are also displayed.

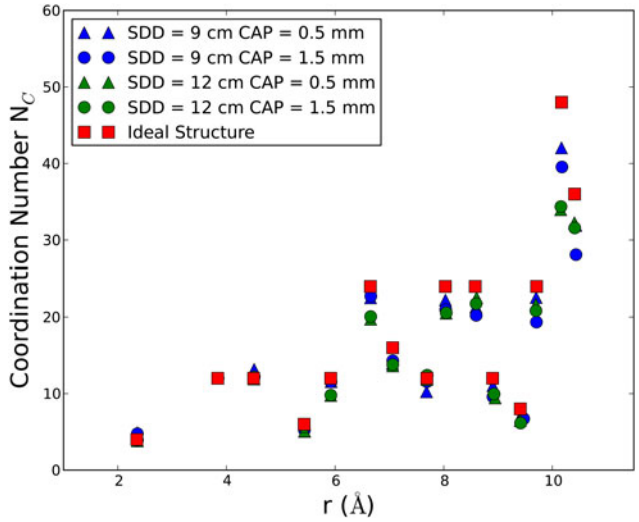

Figure 6. (Colour online) Experimental coordination numbers of silicon NIST SRM 640c obtained by fitting the radial distribution function *R(r)*.

has only eight electrons compared with 56 for Barium, the X-ray data are not sensitive to oxygen; therefore, we have kept the oxygen coordinates fixed and we have refined only cell parameters, Ti-off centering (when present) and isotropic thermal displacement parameters. The instrumental contribution was previously evaluated from Silicon NIST SRM 640c. A much better fit was found for the non-centro symmetric (*P*4*mm*) model compared with the centro-symmetric (*Pm*-3*m*), which confirms that the average structure maintains the polarization (as expected). Moreover, a small amount of a $BaCO_3$ phase impurity was observed and quantified (around 3 wt. %). The graphical fit is displayed in Figure 7, while full results are displayed in Table III.

TABLE II. Average percentage error in silicon coordinations as determined by radial distribution function analysis.

Sample	1–7 Å range	7–11 Å range
SDD = 9 cm CAP = 0.5 mm	10.07	9.85
SDD = 9 cm CAP = 1.5 mm	7.49	15.89
SDD = 12 cm CAP = 0.5 mm	10.27	13.98
SDD = 12 cm CAP = 1.5 mm	8.20	15.15

Different from previous $BaTiO_3$ room temperature investigations (Petkov *et al.*, 2006; Rabuffetti and Brutchey, 2012), our analysis has not provided negative values for the mean-square atomic displacement of oxygen and titanium: this can be attributed to the particle size of our sample (around 100 nm), that does not excessively suppress the Bragg peaks, in contrast with Petkov *et al.*, and with Rabuffetti and Brutchey, where the particle size was at least one order of magnitude smaller. However, the nanometric size motivated us to look for possible local variations in the sample and we therefore moved to pair distribution analysis.

Figure 8 displays the room temperature data of the $BaTiO_3$. In *Q* space, the importance of high statistics (500 images, red curve) compared with single image (blue curve) is shown on the top right side. In real space, spurious ripples are greatly reduced and in spite of the instrumental damping of the signal, the *G*(*r*) has signal up to around 55–60 Å and clear features in the low *r* region as displayed on the bottom left side.

An initial fit of the *G*(*r*) has been performed in the 1.5–45 Å range using the PDFgui program with the tetragonal and the cubic models. We have not considered larger *r* values because of the damping of the signal. Scale factor, cell parameters, Ti-off centering (when present), and isotropic thermal displacement parameters have been refined. Q_{DAMP} and Q_{BROAD} parameters have been fixed from a silicon NIST SMR 640c collected at the same conditions. As expected, the tetragonal model better describes the structure and gives an R_{WP} values of 17.22% compared with 20.53% for the cubic model. However, the fit is not satisfactory, and this suggests that a unique structure is not able to describe our sample in the 1.5–45 Å range. Down to around 15 Å, the tetragonal model works very well and yields good fit (R_{WP} was 13.19%). Full results of PDFGUI fits in the 15–45 Å range are summarized in Table IV.

https://doi.org/10.1017/S0885715617001166 Published online by Cambridge University Press

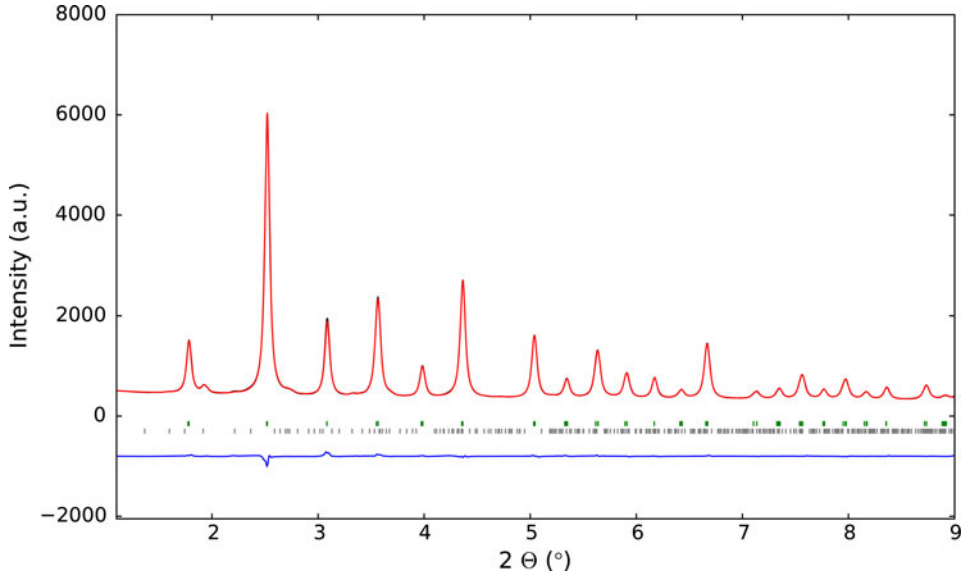

Figure 7. (Colour online) Graphical fit of $BaTiO_3$ Rietveld refinement. HKLs are provided for $BaTiO_3$ (in green) and for $BaCO_3$ (in grey).

TABLE III. $BaTiO_3$ results from Rietveld refinement of the tetragonal and cubic crystallographic models at room temperature.

	P4mm	*Pm-3m*
a (Å)	4.00650 (8)	4.01206 (4)
c (Å)	4.02404 (16)	Equals *a*
z (Ti)	0.5268 (14)	Not present
Ba U_{ISO} (Å^2)	0.0042 (12)	0.00374 (14)
Ti U_{ISO} (Å^2)	0.0032 (5)	0.0072 (2)
O1 U_{ISO} (Å^2)	0.0058 (14)	0.0060 (3)
O2 U_{ISO} (Å^2)	0.0054 (27)	Not present
R_{WP} (%)	0.99	1.31

At lower *r* values, the fit becomes worse, which is an evidence of local structural variations. We focus on the 1.5–15 Å range to highlight differences between the local and average structure. If the tetragonal crystallographic modification is refined in the 1.5–15 Å range, the local model has larger tetragonality (*c*/*a* axis ratio) and smaller Ti displacements. This is counterintuitive because it is hard to understand how a lattice is more metrically elongated with a reduced local displacement of the titanium atom. Similar findings were shown by previous authors (Smith *et al.*, 2008; Rabuffetti and Brutchey, 2012) which concluded that the local crystal structure is less sensitive to disorder than the average structure, leading to abnormally high values of *c*/*a* in the low range. Unless there is some difference in the samples, these controversial results indicate that the tetragonal structure is not right for the local structure here. The Ti thermal isotropic displacement parameter is 65% larger at low *r* than in the 15–45 Å range, which suggests Ti-off centering is not only in the *c* direction but actually off-axis. If the symmetry is

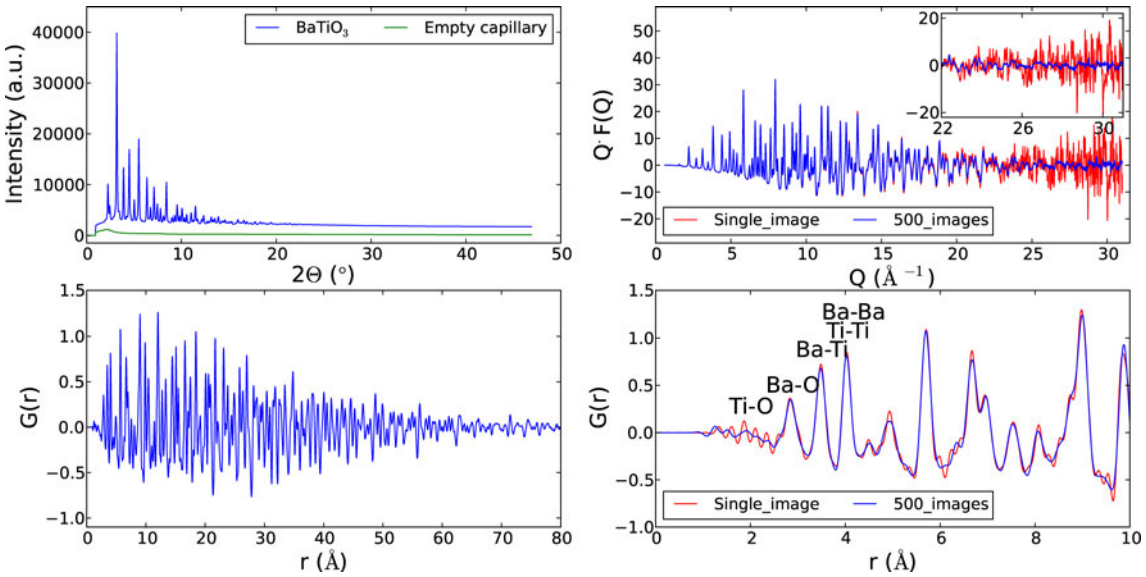

Figure 8. (Colour online) PDF data of the investigated $BaTiO_3$. Top left: raw data (sample in blue, empty capillary in green). Top right: reduced total scattering function *Q.F(Q)* for 1 single vs 500 images with a magnified inset for the high Q region. Bottom left: *G(r)* in the 0–80 Å range. Bottom right: *G(r)* is plotted in the local 1–7.2 Å range for 1 single vs 500 images.

https://doi.org/10.1017/S0885715617001166 Published online by Cambridge University Press

TABLE IV. $BaTiO_3$ pair distribution function results in the average region (15–45 Å range).

	*P*4*mm*	*Pm*-3*m*	*P*4*mm* plus orthorhombic distortion
a (Å)	4.02557	4.03244	4.02333
b (Å)	Equals *a*	Equals *a*	4.0266
c (Å)	4.04852	Equals *a*	4.04874
z (Ti)	0.525211	Not present	0.520172
y (Ti)	Not present	Not present	Equals *z* (Ti)
Ba U_{ISO} (Å^2)	0.0041	0.0049	0.0042
Ti U_{ISO} (Å^2)	0.0050	0.0086	0.0036
O U_{ISO} (Å^2)	0.0162	0.0175	0.0149
R_{WP} (%)	13.19	15.23	13.68

TABLE V. Pair distribution function results in the local region (1.5–15 Å range).

	*P*4*mm*	*Pm*-3*m*	*P*4*mm* plus orthorhombic distortion	*Pm*44 constrained
a (Å)	4.01819	4.03225	4.02116	4.02554
b (Å)	Equals *a*	Equals *a*	4.0144	Equals *a*
c (Å)	4.06144	Equals *a*	4.06213	4.04616
z (Ti)	0.51772	Not present	0.519975	0.527393
y (Ti)	Not present	Not present	Equals *z*	Not present
Ba U_{ISO} (Å^2)	0.0031	0.0034	0.0032	0.0037
Ti U_{ISO} (Å^2)	0.0073	0.0088	0.0041	0.0041
O U_{ISO} (Å^2)	0.0249	0.0222	0.0237	0.0233
R_{WP} (%)	18.14	20.08	17.82	18.78

reduced to an orthorhombic modification, we have observed that (i) the Ti thermal isotropic displacement parameter is halved and (ii) the fit is improved. Fit results for 1.5–15 Å range are summarized in Table V. This improvement no longer manifests in the average range (i.e. 15–45 Å), as a confirmation that the average structure is well described by the tetragonal modification.

Considering these results, our $BaTiO_3$ sample displays an average tetragonal structure, which has a local orthorhombic-like distortion on length scales of about four unit cells. Further lowering of the local symmetry might improve the fit in the 1.5–15 Å range. Moreover, the use of $G(r)$ obtained by averaging 500 images instead of using one single image improved the PDFGUI fit, lowering the R_W from 22 to 18 wt. %. Further information, from neutron diffraction (for oxygen), or electron microscopy or from modeling approaches, might all be included in a future study.

D. Glass with crystalline phase impurity

For each of the nine samples including quartz, five different volumes in the sample have been irradiated by the beam. For each volume of each sample, 500 images were averaged to improve the statistics. At this level, for each sample, the median between the five different images were generated, in order to remove/reduce the spots generated by single-crystal diffraction of quartz grains. Finally, for each sample, the median image was azimuthally integrated using pyFAI. A threshold value to get a successful removal of quartz spots was found: when the quartz amount is lower/equals to about 2.5 wt. %, the median filtering works well, providing a 2θ vs. intensity pattern that is substantially identical to the pattern of pure glass. On contrary, this was not the case when quartz amounts were larger than 2.5 wt. %. This effect is displayed in Figure 9.

For data with quartz amounts <2.5 wt. %, the data were processed with GudrunX, to get the $F(Q)$ and the $g(r)$ of the samples, and afterwards an empirical potential structure

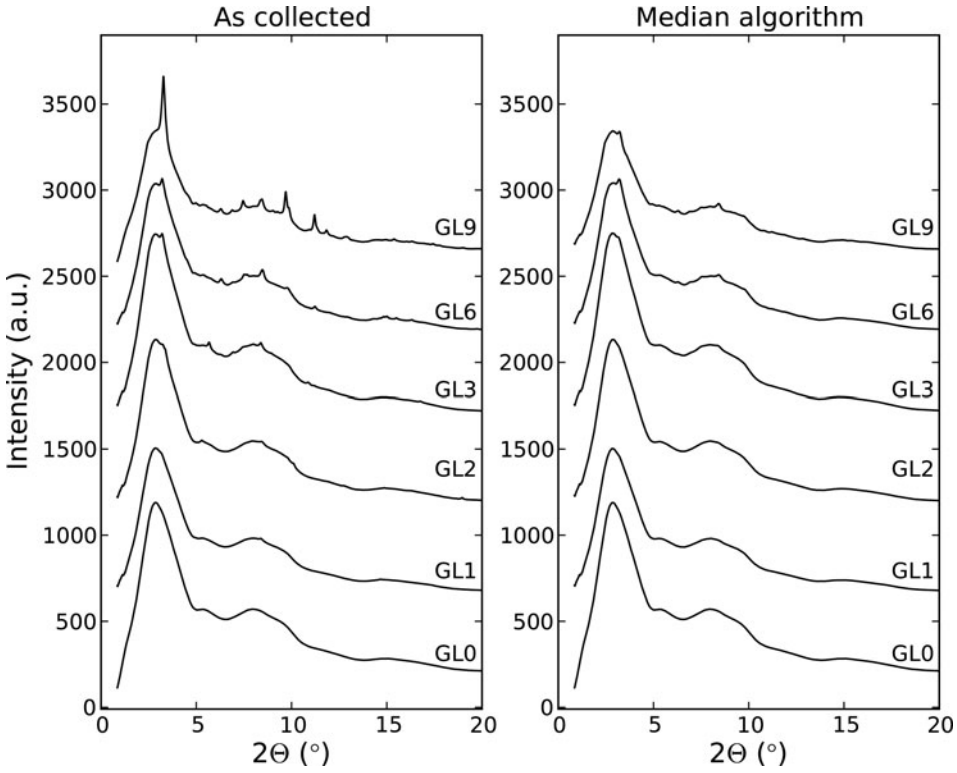

Figure 9. 2θ vs intensity pattern of glass samples with different quartz amounts. On the left side, as collected pattern are displayed while on the right side the median filtering has been applied to reduce Bragg signal from quartz.

https://doi.org/10.1017/S0885715617001166 Published online by Cambridge University Press

refinement (EPSR, Soper, 2010a,b) was applied to evaluate whether the median filtering was successful even when extracting structural information from the diffraction pattern. The same potentials of Bernasconi *et al.* (2016) were used. Non-bridging oxygen (NBO) fractions, which represent the fraction of oxygen shared by one single structural unit [i.e. silicon and aluminum centered tetrahedra (Shelby, 2005)], have been used as a criterion to compare the samples. NBO fractions of 0.136, 0.133, and 0.126 have been found for samples GL0, GL1, and GL2, respectively. This trend towards lower NBO fractions can be attributed to some parasitic signals from the crystalline phase: the larger the signal, the more ordered and polymerized is the structure. These results underline that, for the present case of interest, the median filtering is not completely successful, but at the same time, this underlines the sensitivity of the data and the modeling approach to weak Bragg/diffuse scattering contributions. The effect of these Bragg/diffuse scattering contributions can be minimized by reducing the capillary size and or the beam size, with the drawback that statistics will be worse and, in turn, the EPSR reproducibility will be even worse, in a similar manner remarked by Bernasconi *et al.*, 2016. Making a step-wise rotation of the sample to change the pattern of single-crystal diffraction spots might also help, but nevertheless, the diffuse background from the crystalline material can never be removed. Increasing the quartz content of the sample does indeed reduce the overall NBO of the sample, in line with our observation.

IV. CONCLUSIONS

The effect on the reciprocal space resolution of different parameters like sample to detector distance, sample thickness, beam size, detector PSF, energy and bandpass ($\Delta E/E$) have been evaluated and computed after geometrical derivation by Eq. (6). The effect of two of these parameters (sample to detector distance and sample thickness) have been then experimentally measured at a high-energy beamline on a silicon NIST SRM 640c and compared with calculations by Eq. (6), showing satisfactory results. The analysis has been extended to real space, where an increase of Q-range is the most desirable requirement after a previous evaluation of PDF damping, an effect that can be reduced by a narrower capillary. This is most important for crystalline samples which have structured $G(r)$ at high r values. For amorphous glasses, the $G(r)$ is anyway rather smooth at high r and so a larger diameter capillary helps to improve counting statistics.

Applications in materials science are illustrated by nano-sized $BaTiO_3$ (particle size around 100 nm) and an aluminosilicate-based glass sample with different crystalline phase additions.

(i) For the $BaTiO_3$, the combination of reciprocal and real space analyses assigned an average tetragonal structure up to around 15 Å, with a lower local symmetry (orthorhombic at least) in the local r-range region. This kind of analysis of local vs. long range structures helps us to understand material properties that conventional structural approaches do not reveal.

(ii) For the glass, it has been possible to remove the contribution of a crystalline phase Bragg contribute, with an underestimation in the NBO fractions of about 0.003, when the addition is around 1.2 wt. %, and of about 0.01, when the addition is around 2.5 wt. %. With this case, besides demonstrating how high-energy diffraction measures the local structure of a glass, we have shown a method to reduce the effects of an undesired crystalline phase.

Acknowledgements

The authors thank the ESRF for the provision of synchrotron beamtime. The authors also thank the anonymous referees for their constructive suggestions.

Bernasconi, A., Diella, V., Marinoni, N., Pavese, A., and Francescon, F. (**2012**). "Influence of composition on some industrially relevant properties of traditional sanitary-ware glaze," Ceram. Int. **38**, 5859–5870.

Bernasconi, A., Wright, J., and Harker, N. (**2015**). "Total scattering experiments on glass and crystalline materials at the ESRF on the ID11 beamline," Powder Diffr. **30**, S2–S8.

Bernasconi, A., Dapiaggi, M., Bowron, D., Ceola, S., and Maurina, S. (**2016**). "Aluminosilicate-based glasses structural investigation by high-energy X-ray diffraction," J. Mater. Sci. **51**, 8845–8860.

Bhalla, A. S., Gou, R., and Roy, R. (**2000**). "The perovskite structure: a review of its role in ceramic science and technology," Mater. Res. Innov. **4**, 3–26.

Cesar da Silva, J., Pacureanu, A., Yang, Y., Bohic, S., Morawe, C., Barrett, R. and Cloetens, P. (**2017**). "Efficient concentration of high-energy x-ray for diffraction-limited imaging resolution," Optica **4**(5), 492–495.

Chandler, C. D., Roger, C., and Hampden-Smith, M. J. (**1993**). "Chemical aspects of solution routes to perovskite-phase mixed-metal oxides from metal-organic precursors," Chem. Rev. **93**, 1205–1241.

Coelho, A. A. (**2005**). Topas-Academic Users Manual. Version 4.1.

Egami, T. and Billinge, S. J. L. (**2003**). *Underneath the Bragg peak: structural analysis of complex material* (Pergamon, Amsterdam, The Nederland).

Farrow, C. L., Juhas, P., Liu, J. W., Bryndin, D., Bozin, E. S., Bloch, J., Proffen, Th., and Billinge, S. J. L. (**2007**). "PDFfit2 and PDFgui: computer programs for studying nanostructure in crystals," J. Phys. Condens. Matter **19**, 335219.

Hall, M. M. Jr., Veeraraghavan, V. G., Rubin, H., and Winchell, P. G. (**1977**). "The approximation of symmetric X-ray peaks by Pearson type VII distributions," J. Appl. Crystallogr. **10**, 66–68.

Holton, J. M., Nielsen, C., and Frankel, K. A. (**2012**). "The point-spread function of fiber-coupled area detectors," J. Synchrotron Radiat. **19**, 1006–1011.

Jeong, I.-K., Heffner, R. H., Graf, M. J., and Billinge, S. J. L. (**2003**). "Lattice dynamics and correlated atomic motion from the atomic pair distribution function," Phys. Rev. B **67**, 104301.

Juhas, P., Davis, T., Farrow, C. L., and Billinge, S. J. L. (**2013**). "PDFgetx3: a rapid and highly automatable program for processing powder diffraction data into total scattering pair distribution functions," J. Appl. Crystallogr. **46**, 560–566.

Kieffer, J. and Wright, J. (**2013**). "PyFAI: a Python library for high performance azimuthal integration on GPU," Powder Diffr. **28**, S339–S350.

Kirkpatrick, P. and Baez, V. (**1948**). "Formation of optical images by X-rays," J. Opt. Soc. Am. **38**, 766–774.

Kwei, G. H., Lawson, A. C., Billinge, S. J. L., and S. W. Cheong (**1993**). "Structures of the ferroelectric phases of the barium titanate," J. Phys. Chem. **97**, 2368–2377.

Labiche, J. C., Mathon, O., Pascarelli, S., Newton, M. A., Ferre, G. G., Curfs, C., Vaughan, G., Homs, A., and Carreira, D. F. (**2007**). "Invited article: the fast readout low noise camera as a versatile x-ray detector for time resolved dispersive extended x-ray absorption fine structure and diffraction studies of dynamic problems in materials science, chemistry, and catalysis," Rev. Sci. Instrum. **78**, 091301–091311.

Norby, P. (**1997**). "Synchrotron powder diffraction using imaging plates: crystal structure determination and Rietveld refinement," J. Appl. Crystallogr. **30**, 21–30.

Petkov, V., Gateshki, M., Niederberger, M., and Ren, Y. (**2006**). "Atomic-scale structure of nanocrystalline $Ba_xSr_{1-x}TiO_3$ (x=1,0.5,0) by X-ray diffraction and the atomic pair distribution function technique," Chem. Mater. **18**, 814–821.

https://doi.org/10.1017/S0885715617001166 Published online by Cambridge University Press

Proffen, T., Page, K. L., McLain, S. E., Clausen, B., Darling, T. W., TenCate, J. A., Lee, S. Y., and Ustundag, E. (**2005**). "Atomic pair distribution function analysis of materials containing crystalline and amorphous phases," Z. Kristallogr. **220**, 1002–1008.

Rabuffetti, F. A. and Brutchey, R. L. (**2012**). "Structural evolution of BaTiO3 nanocrystals synthesized at room temperature," J. Am. Chem. Soc. **134**, 9475–9487.

Shelby, J. (**2005**). *Introduction to Glass Science and Technology* (RSC, Cambridge).

Smith, M. B., Page, K., Siegrist, T., Redmond, P. L., Walter, E. C., Seshadri, R., Brus, L. E., and Steigenwald, M. L. (**2008**). "Crystal structure and the paraelectric-to-ferroelectric phase transition of nanoscale $BaTiO_3$," J. Am. Chem. Soc. **130**, 6955–6963.

Snigirev, A., Snigireva, I., Grigoriev, M., Yunkin, V., Di Michiel, M., Vaughan, G. & Kohn, V, and Kuznetsov, S. (**2009**). "High energy X-ray nanofocusing by silicon planar lenses," J. Phys. Conf. Ser. **186**, 012072.

Soper, A. K. (**2010a**). "*GudrunN and GudrunX: Programs for Correcting Raw Neutron and X-ray Diffraction Data to Differential Scattering Cross Section* (ISIS Disordered Material Group, Didcot, UK).

Soper, A. K. (**2010b**). *EPSRshell: A Users Guide* (ISIS Disordered Material Group, Didcot, UK).

Vaughan, G., Wright, J., Bythkov, A., Rossat, M., Gleyzolle, H., Snigireva, I., and Snigirev, A. (**2011**). "X-ray transfocators: focusing devices based on compound refractive lenses," J. Synchrotron Radiat. **18**, 125–133.

Wu, G., Rodrigues, B. L., and Coppens, P. (**2002**). "The correction of reflection intensities for incomplete absorption of high-energy x-rays in the CCD phosphor," J. Appl. Crystallogr. **35**, 356–359.

Yavari, A. R., Le Moulec, A., Inoue, A., Nishiyama, N., Lupu, N., Matsubara, E., Botta, W. G., Vaughan, G., Di Michiel, M., and Kvick, A. (**2005**). "Excess free volume in metallic glasses measured by X-ray diffraction," Acta Mater. **53**, 1611–1619.